ELSEVIER

Contents lists available at ScienceDirect

# Materials & Design

journal homepage: www.elsevier.com/locate/matdes



# Ultrasonic effects on gas tungsten arc based wire additive manufacturing of aluminum matrix nanocomposite



Tianzhao Wang, Veronika Mazánová, Xun Liu\*

Welding Engineering Program, Department of Materials Science and Engineering, The Ohio State University, 1248 Arthur Adams Drive, Columbus, OH 43221, United States

#### HIGHLIGHTS

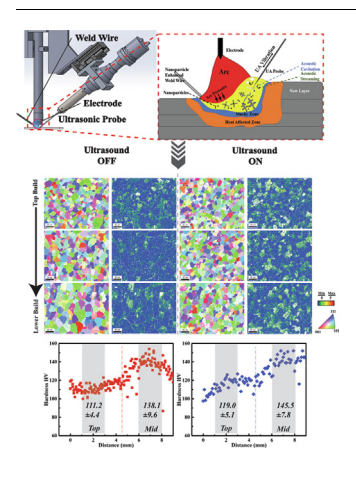
- An innovative ultrasonically assisted wire arc additive manufacturing process was first developed for the fabrication of AA7075 metal matrix nanocomposite.
- The ultrasonic probe is directly immersed in the local deposition pool, greatly increasing the energy efficiency compared with existing methods.
- Synergistic effects of ultrasound and nanoparticles modified the solidification process and refined the microstructure, which enhance mechanical properties.
- Acoustic streaming and cavitation effects induced by ultrasound in the molten pool reduce clustering of nanoparticles.

#### ARTICLE INFO

Article history:
Received 11 October 2021
Revised 21 December 2021
Accepted 6 January 2022
Available online 10 January 2022

Keywords: Wire Arc Additive Manufacturing Ultrasound Metal Matrix Nanocomposite AA7075

#### G R A P H I C A L A B S T R A C T



# ABSTRACT

This study focused on a newly developed ultrasonically assisted (UA) wire arc additive manufacturing (WAAM) process for metal matrix nanocomposite of AA7075 with TiB<sub>2</sub> nanoparticles. The ultrasonic probe was directly dipped into the local molten pool and traveled behind the arc during deposition. Comprehensive experimental studies were performed and the UA-WAAM sample showed superiorities over conventional WAAM ones in multiple perspectives including a lower number of porosities, refined solidification structure, and less agglomerated nanoparticle distribution under the same deposition parameters. These improved microstructure features led to enhanced mechanical properties of the UA-WAAM samples, as reflected in the tensile tests and hardness measurement results. The benefits of nanoparticles in the formation of equiaxed grain structures and strength contribution was further leveraged by UA based on their better dispersion. The ultrasonic effects on WAAM process can be mainly attributed to the two nonlinear physical phenomena: acoustic cavitation and streaming induced by power ultrasound in molten metal.

© 2022 The Authors. Published by Elsevier Ltd. This is an open access article under the CC BY license (http://creativecommons.org/licenses/by/4.0/).

#### 1. Introduction

Emphasis on energy and environmental sustainability requires new structural materials with both lightweight and excellent

<sup>\*</sup> Corresponding author. E-mail address: liu.7054@osu.edu (X. Liu).

mechanical performance. Metal matrix nanocomposites (MMNCs), which are based on metal reinforced with nano-sized ceramic particles, provide combined high strength-to-weight ratio and ductility, as well as improved performance at high temperatures. These attractive features of MMNCs make them a promising group of structural materials in the automotive and aircraft industries [1]. The manufacturing processes of MMNCs can be classified into general two groups of in-situ and ex-situ methods. Ceramic nanoparticles are generated via internal reactions in in-situ processes [2,3], while ex-situ methods involve externally adding nanoparticles followed by enforced dispersion. Agglomeration of nanoparticles is one of the main challenges in the fabrication of MMNCs [4]. Moreover, MMNCs fabricated from these methods are limited to products with regular shapes, which require following machining to achieve the required final component geometry. Considering the nanoparticles in the MMNCs directly increase the machining difficulties [5], advanced manufacturing processes that can achieve near-net-shape MMNC products and uniform dispersion of particles are highly desirable.

Compared with traditional manufacturing processes, additive manufacturing (AM) is uniquely advantageous in rapid prototyping of freeform geometries with higher efficiency and lower cost. Novel light-weight structures, for example, lattice structures that can highly contribute to the weight reduction, can be fabricated by AM processes at a much lower cost compared with conventional processes [6]. Wire arc additive manufacturing (WAAM), categorized as direct energy deposition AM process, provides advantages of higher deposition rates, better energy efficiencies, and lower cost compared with powder-based processes [7]. However, WAAM shares the demerits of as-cast microstructure nature: porosities, residual stress, segregation, and solidification cracking along the building direction [8-10]. Inter-pass rolling has been proved to be effective in porosities improvement, grain refinement, and residual stress reduction [11,12]. However, inter-pass cold working also requires a longer processing time and higher fabrication costs.

Metal matrix in MMNC usually selects materials with high specific strength, such as aluminum and magnesium alloys. AA7075 aluminum is commonly used in the aerospace industry with its distinguished strength and fracture toughness. As precipitation hardened aluminum alloy, AA7075 is sensitive to solidification cracking and porosities during melting involved processes, like casting, fusion welding, and additive manufacturing. Stopyra et al. [13] studied the effect of process parameters on the porosity and hot cracking behavior of AA7075 alloy with laser powder bed fusion process. They ascribed the poor processibility of AA7075 to its extended solidification range. Nanoparticles have been added into the aluminum melts and promote improved castability and weldability. It is reported that the hot tearing in cast A206 alloy can be markedly reduced with an addition of 1 wt% Al<sub>2</sub>O<sub>3</sub> nanoparticles [14]. A novel AA7075 MMNC with the addition of TiC nanoparticles that can remarkably improve the weldability of AA7075 was developed. Instead of typical columnar dendrites, refined equiaxed grains were achieved by the addition of TiC nanoparticles [15]. The nano-treated AA7075 welding wires were further employed in laser-based wire additive manufacturing and successfully removed solidification cracking [16].

The combined objectives to mitigate the nanoparticle agglomeration in MMNCs and overcome the limitations with WAAM of AA7075 intrigued the motivation of applying ultrasonic vibration during the WAAM process of AA7075-based MMNCs. High-intensity ultrasound with a frequency of 20 kHz or above has been utilized in ameliorating various molten metal processes for grain refinement and porosities degassing [17]. Besides, ultrasonic energy has been shown to effectively disperse nanoparticles during ex-situ fabrication of MMNC [4]. These benefits are contributed by directly immersing the ultrasonic probe into the molten pool and

are mainly based on two physical phenomena induced by ultrasonic: acoustic cavitation and acoustic streaming effects.

Studies have been performed to employ ultrasonic vibrations to improve additive manufacturing and show promising results. Chen et al. configured the ultrasonic probe next to the WAAM building wall and the vibration was applied perpendicularly to the substrate metal, which indirectly transmitted the high-frequency vibration to the molten pool. Fine cellular microstructure and improved tensile properties were observed [18]. Besides, an ultrasonic-assisted laser powder deposition process was studied, where the ultrasonic energy was implemented from the bottom substrate. Full transition from columnar to equiaxed grains was achieved with UA for both Ti-6Al-4V and Inconel 625 alloys [19]. UA micro-forging technique was applied to the top deposited layer with an offset behind the molten pool during laser and wire additive manufacturing process of Ti alloy and refined solidification structure was also obtained [20,21]. Despite the promising results, these configurations lead to varying vibration amplitudes at different deposition heights. Besides, since the entire structure needs to be vibrated to transmit energy to the local melt pool, the achievable build height is limited by the output power of the UA transducer. Moreover, the ultrasonic energy can also be attenuated along the propagation path. A novel approach during single pass welding of magnesium alloy applied a direct UA probe insertion into the weld pool and showed more effective grain refinement [22]. However, how the direct immersion of the UA probe affects the WAAM process and nanoparticle dispersion has not been cleared yet.

This study focused on a new approach of applying ultrasonic energy during WAAM of AA7075 MMNC, where the probe was directly immersed into the local deposition pool. Based on the newly developed UA-WAAM system, ultrasonic effects on the MMNC mechanical properties and microstructure characteristics at different length scales were comprehensively analyzed.

#### 2. Method

# 2.1. Materials

A  $TiB_2$  nanoparticle enhanced AA7075 weld wire (AA7075 NT, MetaLi LLC) with a diameter of 1.2 mm was employed in the new proposed UA-WAAM process. An AA6061 aluminum plate with a thickness of 19 mm was applied as the substrate.

# 2.2. Ultrasonic assisted (UA)-WAAM experimental system

Fig. 1 shows the schematic of the developed UA-WAAM system, which is based on a Gas Tungsten Arc Welding (GTAW) facility. A non-consumable 1.5% lanthanated tungsten electrode was employed to initiate and maintain the welding arc. The filler metal was fed in front of the arc while the UA probe traveled behind the arc. The UA probe was installed at the end of the UA horn, which was mounted on the welding torch to provide synchronous travel. The location depth of the UA probe was adjusted by the pneumatic cylinder on the UA booster.

#### 2.3. UA-WAAM process

Table 1 summarized the parameters of the UA-WAAM process. A total of 20 layers were deposited onto the substrate with a decreasing heat input at higher layers. The travel speed was 1.5 mm/s with a total travel time of 1 min in each layer. An average height deposition rate of 0.9 mm/pass was maintained throughout the process.

An AC current power supply was employed to balance surface waviness and penetration at the workpiece. During GTAW AC

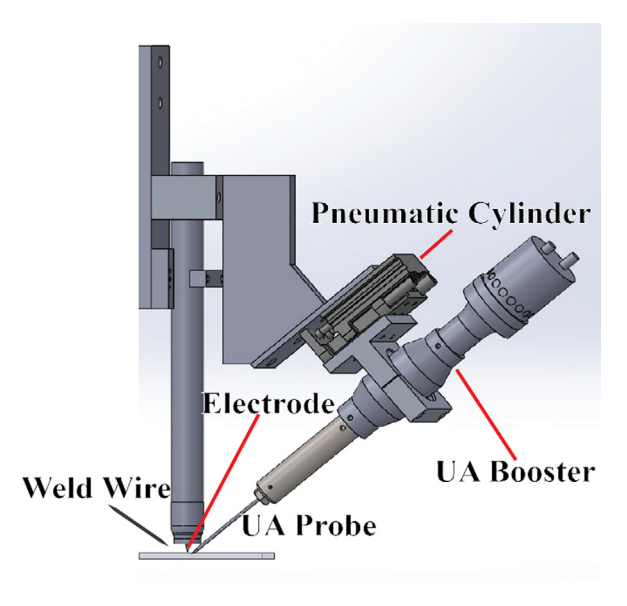


Fig. 1. Schematic illustration of the UA-WAAM system.

cycles of aluminum, the electrode negative polarity (EN) generates a higher amount of heat at the workpiece while electrode positive polarity (EP) assists the workpiece surface cleaning and produces more fusion area [23]. In this study, a 45% EP was assigned to achieve an acceptable building height for each layer without compromising deposition qualities. Heat input was decreased by 10% for every 3  $\sim$  5 passes to avoid excessive penetration and collapse of the newly deposited layer. To maintain a stable arc length, the voltage remained constant while the current was deducted by 10%. Argon shielding gas was applied at a flow rate of 9.5 L/min throughout the entire building process.

The UA probe was inserted after the 10th pass considering the instability induced by probe insertion, which might skew the geometry of the first few layers and introduce undesired difficulties in following depositions. The tip of the UA probe was vibrating at a frequency of 19.90 kHz with an amplitude of 14.6 µm. During the process, the UA probe was brought to a depth of 1 mm below the melt surface and was kept at a constant distance of 2.5 mm behind the arc center. The UA probe was inserted upon the molten pool formation and retracted after 30 secs, which was in the middle of the deposition length. Accordingly, samples fabricated with UA and without UA (no-UA) were obtained in the same building wall at different segments, which provided more representative comparisons under the same process parameters.

# 2.4. Thermal imaging of the UA-WAAM process

Temperature distribution during the UA-WAAM was captured through a non-contact infrared (IR) camera (FLIR A6751sc) at a frame rate of 30 Hz. Each frame had a resolution of  $640\times512$  and a temperature range of 200-2000°C. The temperature distribu-

tion of one single pass with a UA probe inserted and retracted was observed from the top side view.

#### 2.5. Mechanical characterization

Vickers micro-hardness analysis was performed on the polished cross-section of both UA and no-UA samples at 100 g of load on a  $100 \times 100$  µm distanced indent grid. Micro-tensile samples with a gauge length of 1.5 mm and gauge width of 0.3 mm were extracted on the top and middle region of the built wall. Fig. 2 shows the cross-section of build via UA-WAAM and indicates the locations of micro-tensile test sample extractions. The samples were prepared with wire electrical discharge machining (Fancuc 180is-WB EDM), at a cutting speed of 0.10 mm/s. The extracted micro-tensile samples were further ground before testing to remove the EDM quenching effect on the sample surface. Tensile tests at a strain rate of 0.06/s were performed on a customized micro-tensile testing system adapted from Kang et al. [24]. At least five specimens were tested at each location.

# 2.6. Microstructure analysis of cross-section of UA-WAAM builds

All samples were prepared according to standard metallurgical procedures. Scanning electron microscope (SEM) equipped with Energy-dispersive X-ray spectroscopy (EDS) detector was employed to analyze the dispersion and distribution of the  ${\rm TiB_2}$  nanoparticles and secondary phases. EDS mapping and line scanning were performed with a counting rate of 50k counts/sec. Besides, electron backscattered diffraction (EBSD) scanning was also performed at representative regions to observe the microstructure-property relationship. EBSD scanned regions were shown in Fig. 2.

#### 3. Results

#### 3.1. WAAM building geometry and porosity

Overview of the cross-sections of the last 10 layers of the build wall with and without UA was compared in Fig. 2. Within this deposition volume of interest, the built wall was further divided into the top, middle, and no-UA substrate regions, as shown in Fig. 2. In the top region, the maximum width of the no-UA sample was 10.51 mm whereas that of the UA sample was smaller at 8.88 mm. The total building height of the no-UA wall was 16.86 mm. With the ultrasonic vibration applied after the 10th pass, the total building height increased to 19.88 mm. This indicated that UA restrained the lateral spreading of the deposited layers, which contributed to the building height. On the other hand, a steeple-roof feature was observed on the top surface of the UA sample. This was related to the intermolecular adhesive forces between the ultrasonic probe and melt. The adhesive force further propagated along the surface of the melt and prevented it from falling towards the sides of the bead.

Porosity distribution in UA and no-UA samples were compared in Fig. 2. With superimposed UA, the porosity area fraction was measured as 0.8% compared to 1.3% of the no-UA sample in the

**Table 1** Parameters of UA-WAAM Process.

Pass No.	Current (A)	Voltage (V)	Wire Feeding Speed (mm/s)	EP %	UA Status
1	380	12	6.35	45	OFF
2-4	340	12	7.62	45	OFF
5-10	300	12	7.62	45	OFF
11-15	270	12	9.10	45	ON
15-20	240	12	11.22	45	ON

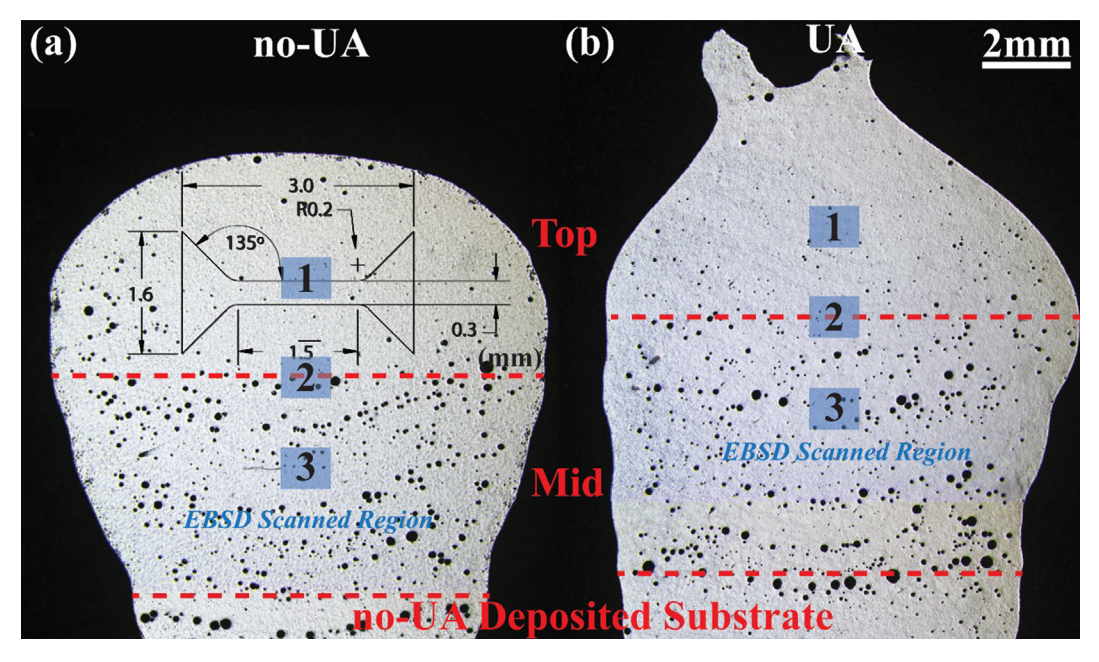


Fig. 2. Overview of transverse cross-section of the last 10 layers of the deposited wall: (a) no-UA and (b) UA segment. Dashed lines indicate the boundaries between the top and middle region. Blue boxes indicate the EBSD scanned regions. Geometry and extraction location of micro tensile test samples were marked with the solid lines in (a). The thickness of the tensile sample was 0.3 mm. (For interpretation of the references to colour in this figure legend, the reader is referred to the web version of this article.)

top region. In the middle region, the porosity area fraction was about 5.0% in both no-UA and UA samples.

#### 3.2. Effect of UA on the weld pool size and heat dissipation

Fig. 3 (a) and (b) show the top side view of the temperature distribution before and after the UA probe insertion into the melt pool. A heat-dissipating path via the UA probe was observed in Fig. 3 (b), where the UA probe in the melt pool acted as a heat sink. Accordingly, the melt pool temperature was slightly reduced, which increased the molten metal viscosity and reduced the fluidity. This can be another factor contributing to the higher height-to-width deposition ratio in the UA sample. Furthermore, as shown in Fig. 3, the penetration was reduced after the UA probe was dipped in the deposition pool. The additional heat dissipation and difference in melt pool size further reduced the reheating effect on previously deposited layers when the UA probe was inserted.

#### 3.3. Effect of UA and nanoparticles on grain structure

Inversed pole figure (IPF) maps in Fig. 4 (a) and (c) show the grain size and grain morphology in UA and no-UA samples. In contrast to the typical columnar or cellular microstructure in conventional fusion welds of aluminum alloys, highly equiaxed grain structures were observed in both UA and no-UA samples. This is consistent with the results in previous works and can be ascribed to the addition of nanoparticles [15]. The grains size is generally larger in the lower layers than the top layers, which is a result of grain growth due to the repeated thermal cycles from following depositions.

Generally, the microstructure was more refined in the UA condition compared with the conventional condition in all scanned regions. Quantification analysis results of grain size distribution were provided in Fig. 5. In region 1, the UA sample showed an average grain size of 21.6  $\pm$  7.8  $\mu m$  while that for the no-UA sample was 23.7  $\pm$  8.8  $\mu m$ . In lower layers region 2, the average grain size was 22.8  $\pm$  7.5  $\mu m$  in the UA sample whereas a slightly coarser average of 25.7  $\pm$  9.3  $\mu m$  was observed in no-UA samples. Moving further lower to region 3, the UA sample had a similar average size of

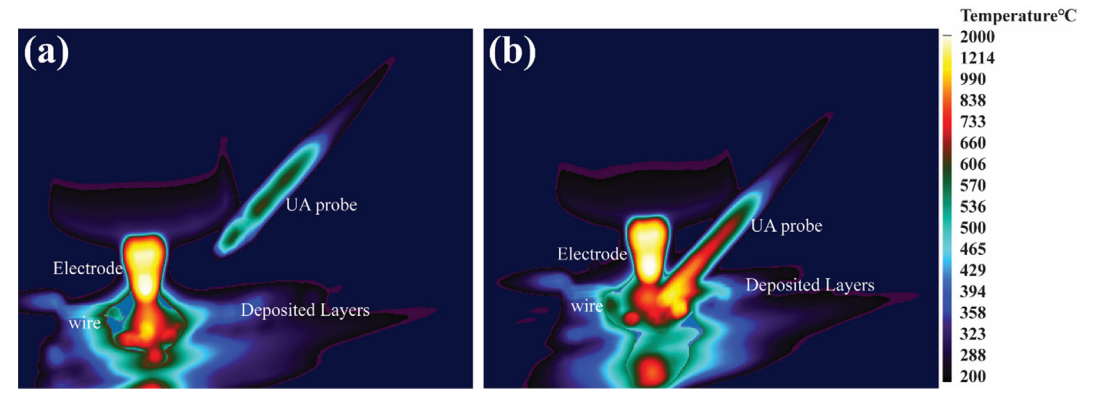
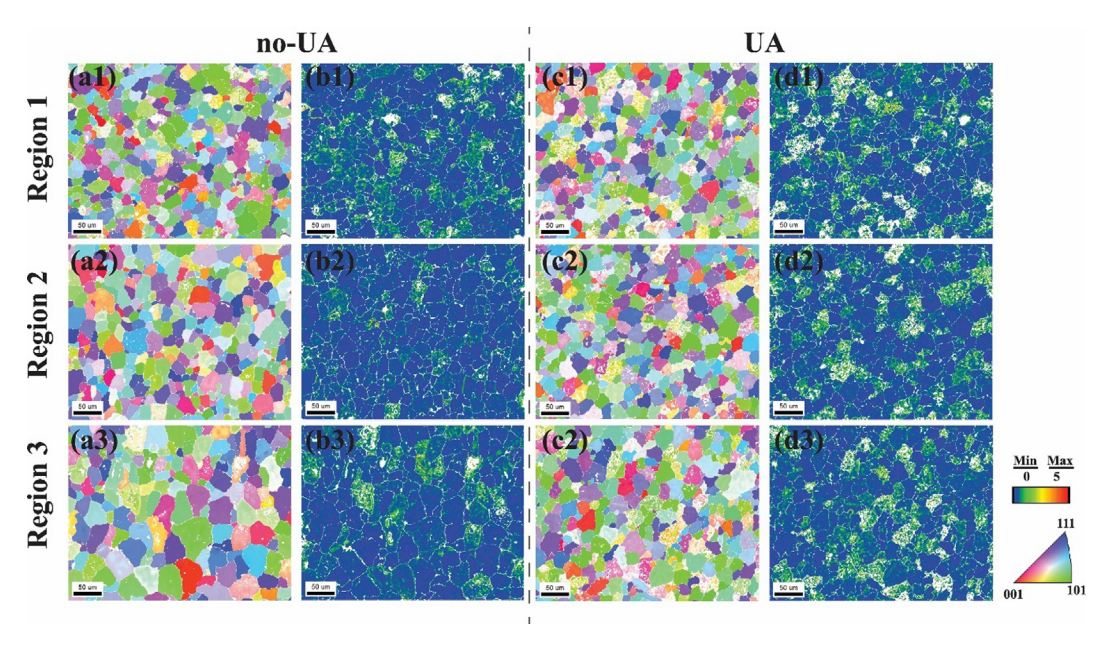


Fig. 3. Top side view of the temperature distribution during UA-WAAM process when (a) UA probe was retracted and (b) UA probe was inserted.



**Fig. 4.** Inversed Pole Figure (IPF) maps of (ax) no-UA and (cx) UA segments, Kernel Average Misorientation (KAM) maps of (bx) no-UA and (dx) UA segments. The x corresponds to the EBSD scanned region designated in Fig. 2. White spots in both IPF and KAM maps indicate a scanned point with confidence index (CI) values lower than 0.15.

 $24.8 \pm 9.3~\mu m$  while significant grain growth was found in the no-UA sample with an average of 35.2  $\pm$  12.1  $\mu m$ . The UA sample showed a consistent grain structure throughout the deposited layers without obvious grain growth while a much coarser grain structure was observed in the lower region (region 3) in the no-UA sample.

#### 3.4. Effect of UA on dispersion of nanoparticles

Backscattered electron (BSE) SEM images around region 2 (see Fig. 2) of the deposited wall are shown in Fig. 6 (a) and (b). It can be observed that majority of the secondary phases in both no-UA and UA samples were preferentially located along the grain boundaries. Higher magnified views of the secondary phases were provided in Fig. 6 (c) and (d) respectively, which corresponded to two types. Large agglomerates were found in the no-UA sample while for the UA sample only serrated-shaped precipitates were found. To analyze their chemical composition, EDS analysis was performed. Fig. 6 (e) and (f) show the EDS line-scan elemental profiles of aluminum (Al), zinc (Zn), magnesium (Mg), silicon (Si), titanium (Ti), and iron (Fe) across the secondary phases. Corresponding positions and paths of the EDS line-scans were marked by arrows in Fig. 6 (c) and (d). In the UA sample in Fig. 6 (f), the elemental profile from EDS line-scan analysis showed enrichments in Mg and Zn, indicating the presence of Mg<sub>x</sub>Zn<sub>v</sub> phases. It was previously reported to be MgZn<sub>2</sub> in AA7075 alloy treated with TiC nanoparticles [15]. The elemental profile of Ti revealed the presence of TiB2 nanoparticle clusters, accumulating around the Mg<sub>x</sub>Zn<sub>v</sub> phases. This distribution can be related to the lattice mismatch between TiB<sub>2</sub> nanoparticles and Mg<sub>x</sub>Zn<sub>y</sub> phase, which provides a more coherent interface and is similar to the distribution mechanism of MgZn<sub>2</sub> and TiC [15]. The presence of these large lamellar eutectic MgxZnv compounds decorated with TiB2 nanoparticles is in accordance with the previous studies of nanoparticles enhanced AA7075 weld wire [16]. In the no-UA sample in Fig. 6 (e), the particle was highly enriched in Ti compared with Mg and Zn elements, indicating the severe agglomeration of TiB<sub>2</sub> nanoparticles. Fe signal was also detected at a noticeable level

overlapped with Mg signal, suggesting the presence of  $Mg_xFe_y$  precipitates.

To further reveal the compositions of the large aggregated clusters observed in the no-UA sample at a triple junction of grain boundaries in Fig. 6 (c), EDS element mapping was performed and presented in Fig. 7. A strong signal of Ti was detected in most of the clustered area, representing large TiB<sub>2</sub> nanoparticle agglomerates with the size of around 20  $\mu m$ . Signals of Mg and Zn were detected at regions in between the TiB<sub>2</sub> clusters. A slight segregation of Si was also observed at the matrix/cluster boundaries. Therefore, the aggregated secondary phases in Fig. 6 (c) mainly consist of TiB<sub>2</sub> nanoparticles. TiB<sub>2</sub> aggregated with a large size in this range were only observed in the no-UA condition. This is distinctly different from the UA sample, where generally the nanoparticles are decorating the secondary precipitates, e.g.  $Mg_xZn_y$ , in the AA7075 matrix instead of being self-clustered into agglomerates.

Besides, white spots represent scanned points with low confidence index (CI) values, which means the diffraction patterns in these points have a low fit with the standard Kikuchi pattern of surrounding orientations. This is different from low-quality sample preparation, which results in a uniform distribution of low CI throughout the whole area. In the condition of the current study, grain boundaries, secondary phases, and local strains can contribute to these difficulties in indexing. Local strains induce the lattice distortion and cause misfits of Kikuchi patterns in certain points [26]. Thus, the UA sample presented a higher level of local strains and a consistent distribution of local strains in the three scanned regions compared with the no-UA one.

# 3.5. Effect of UA on grain orientation distribution

EBSD analysis also provided information of local misorientation as shown in Fig. 4 (c) and (d). The Kernel average misorientation (KAM) maps represent the average local misorientation of adjacent pixels. Higher KAM values indicate larger local misorientation angle and higher geometrically necessary dislocation (GND) density, as expressed in the following equation [25]:

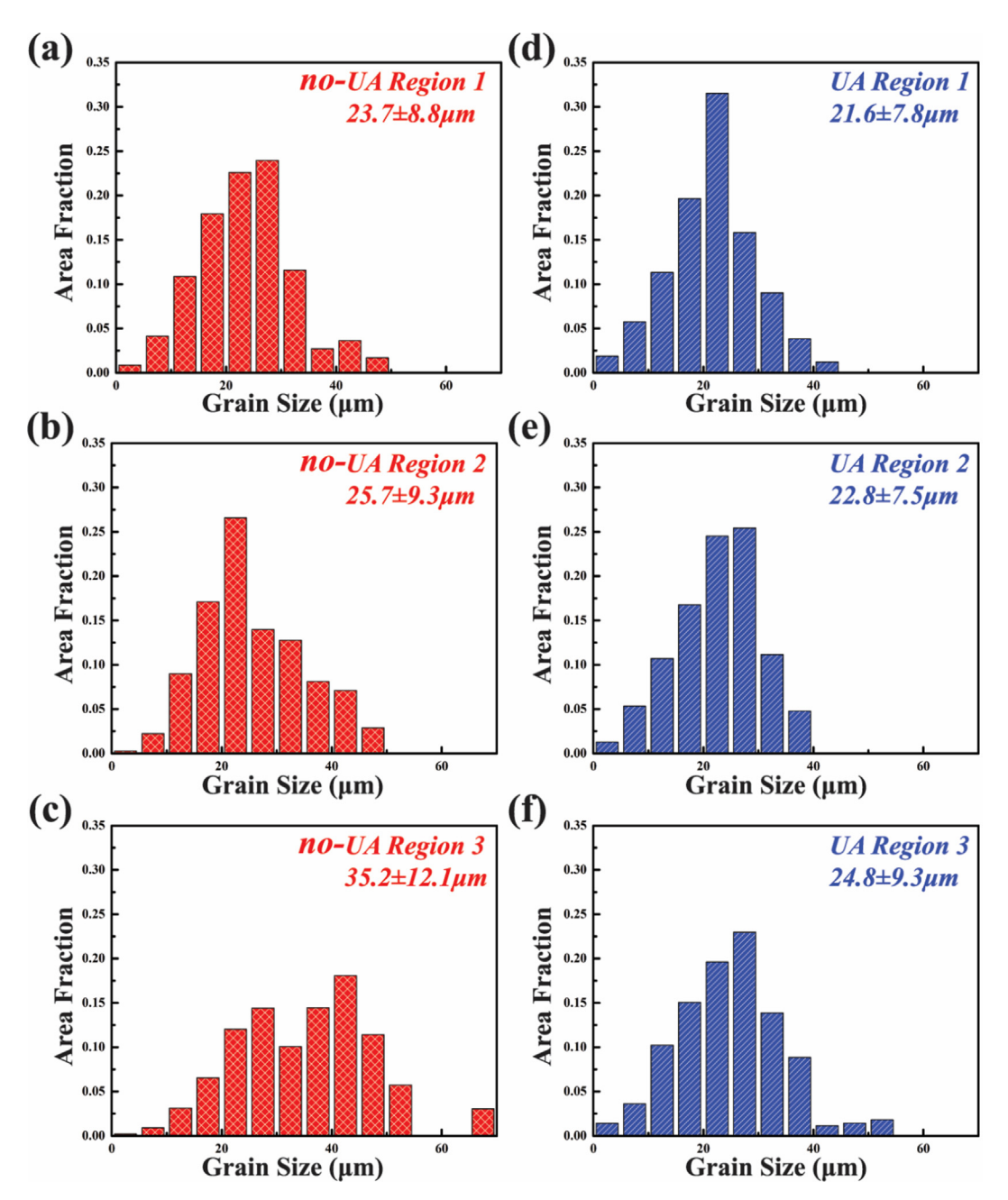


Fig. 5. Statistical analysis of grain size distribution in region 1 in (a) no-UA sample and (d) UA sample, region 2 in (b) no-UA sample and (e) UA sample, and region 3 in (c) no-UA sample and (f) UA sample. Region numbers correspond to the region designation in Fig. 2.

$$\rho = \alpha \frac{\mathit{KAM}}{b \cdot \mathit{R}}$$

Where  $\rho$  is the GNDs density,  $\alpha$  is a constant, b is the magnitude of the Burgers vector and R is the Kernel size. Compared with the no-UA sample, the UA one showed a higher level of KAM distribution in Fig. 4 (d). In lower regions (regions 2 and 3), a decreasing of KAM levels in both no-UA and UA were observed. Different from slightly decreasing KAM values in the UA sample, the no-UA sample showed a more notable drop when moving to lower regions.

# 3.6. Effect of UA on mechanical properties

Fig. 8 (a) and (b) shows the hardness line scanning paths and mapping regions in no-UA and UA samples of the last 10 layers. Fig. 8 (c) and (d) compare the micro-hardness line distribution

between no-UA and UA samples. Starting from the top surface of the build, the hardness increased and reached the maximum value in the middle region, then slightly decreased only in the no-UA sample. Grey windows indicate the top and middle region corresponding to the sample-extraction locations of micro-tensile tests. Local hardness of top and middle regions was calculated and presented in the grey window. An average hardness of 111.2  $\pm$  4.4 in the top region and 138.1  $\pm$  9.6 in the middle region were calculated in the no-UA sample, while the UA sample shows a higher average hardness of 119.0  $\pm$  5.1 in the top region and 145.5  $\pm$  7.8 in the middle region. The higher hardness in the middle region can be attributed to the artificial aging of the precipitates in the AA7075 metal matrix due to the repeated thermal cycles during top layer depositions. Fig. 8 (e) and (f) show the hardness mapping results, the UA

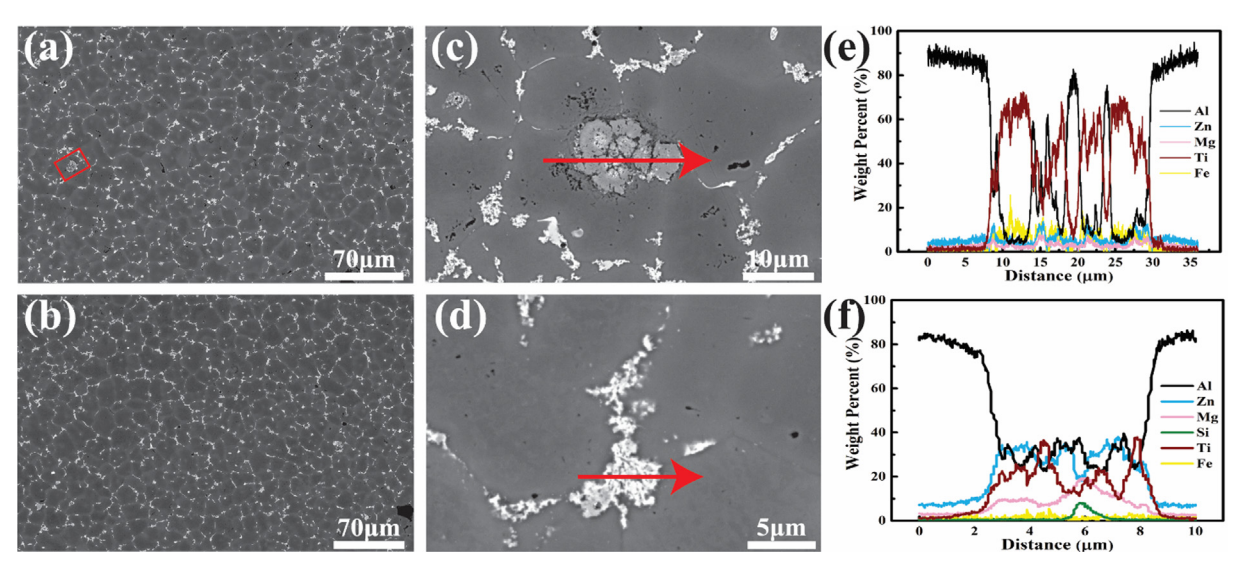


**Fig. 6.** BSE-SEM images acquired in the top region of (a) no-UA sample and (b) UA sample. SEM images of precipitates at grain boundaries in (c) no-UA sample (indicated by red window in (a)) and (d) UA sample. EDS line scanning results of (e) no-UA sample and (f) UA sample, of which the scanning paths are indicated by red arrows in (c) and (d). (For interpretation of the references to colour in this figure legend, the reader is referred to the web version of this article.)

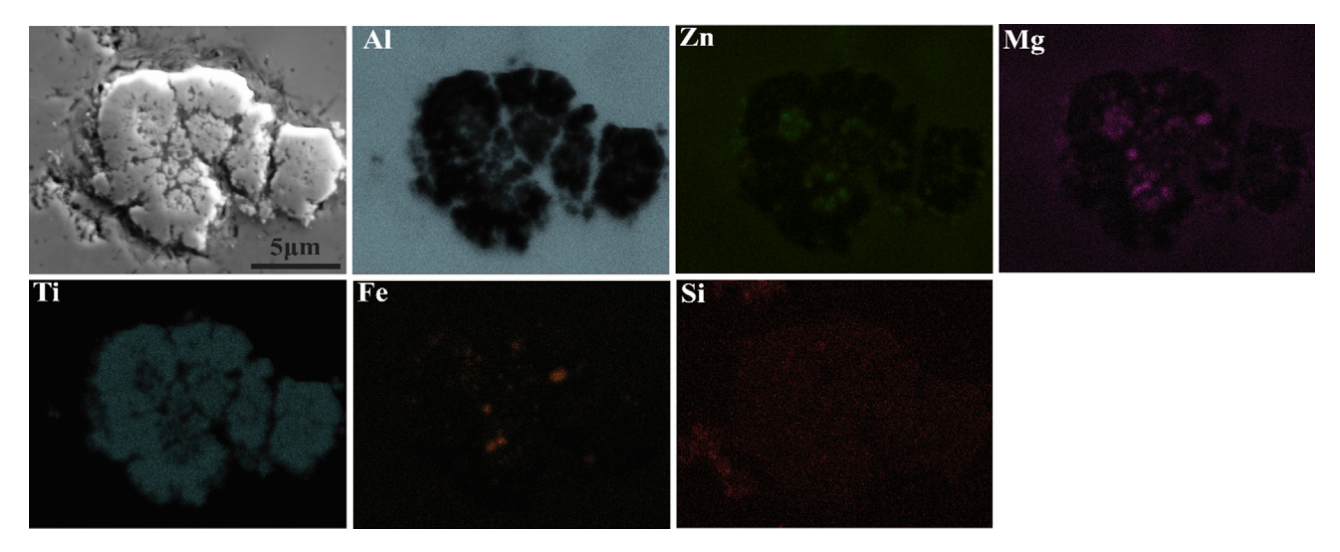


Fig. 7. EDS mapping of the large clusters in no-UA sample. The secondary electron image shows the morphology of the cluster.

sample exhibits a more homogeneous and harder structure than the no-UA one, which is compatible with the line scanning results.

Fig. 9 compared the micro-tensile test results of the samples extracted from the top and middle region of UA and no-UA samples and the specific orientations are shown in Fig. 2. Defects-induced variations exist among individual micro-tensile samples considering their small sizes. In the top region, both tensile strength and elongation of the UA samples were higher than no-UA samples. Averaged tensile strength of about 296.38 ± 14.08 MPa and elongation of 11.35 ± 3.4 % were achieved in the UA condition, whereas those for no-UA samples were 203.2  $\pm$  32.275 MPa and 8.2  $\pm$  0.22 %. Both UA and no-UA samples extracted from the middle region showed higher strength than those extracted from the top region, being consistent with the hardness results. UA samples presented a tensile strength of 311.8  $\pm$  23.07 MPa and an elongation of 9.3  $\pm$  2.3 % whereas those for no-UA samples were 296.2  $\pm$  51.84 MPa and  $7.2 \pm 0.45$  %, respectively. It can be noticed that the average strength of UA samples is similar to the no-UA ones whereas the ductility is slightly higher.

# 4. Discussions

Since the UA-WAAM system utilized the ultrasonic probe directly immersed in the local molten pool during the deposition process, the small volume of melt enabled efficient ultrasonic energy propagation to induce acoustic cavitation and streaming effects, which accordingly modified the solidification behavior in various perspectives. The improved microstructure finally led to enhanced mechanical properties.

#### 4.1. Porosity reduction

Ultrasonic degassing has been widely applied in casting industries of aluminum alloys to remove porosities. During the UA-WAAM of the aluminum nanocomposite in this study, it is noteworthy that both the ultrasonic energy and nanoparticles are involved in the degassing process. Nonmetallic particles, which in this material system are mainly TiB<sub>2</sub> nanoparticles and other inclusions, serve as hydrogen concentrators and cavitation nuclei and decrease the cavitation threshold. The concentration of non-

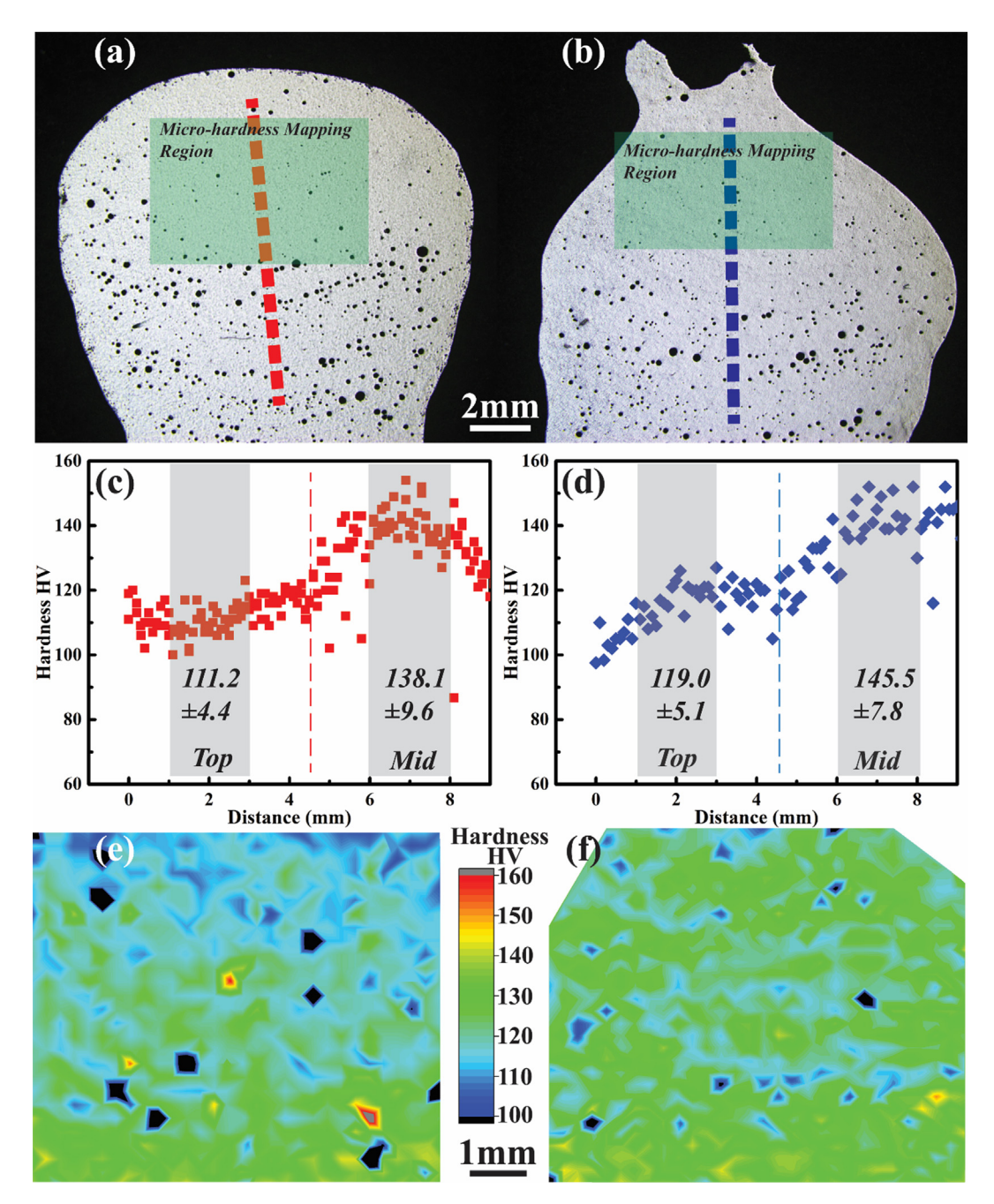


Fig. 8. Hardness line scan path and hardness mapping region in (a) no-UA sample and (b) UA sample. Hardness line scanning results on the (c) no-UA sample and (d) UA sample with local average hardness in the top and middle region presented. Hardness maps of the top and middle region in (e) no-UA sample and (f) UA sample.

metallic nuclei critically influences cavitation development. Under the sinusoidal acoustic pressure field from UA, the cavitation bubbles initiate at non-wettable particles in the melt and transform into gaseous bubbles [27]. UA-induced cavitation pulsation directs hydrogen diffusion into the gaseous bubbles via rectified diffusion and enhances the bubble expansion. A certain fraction of these bubbles collapse in the high-pressure cycle and produce shock waves, whereas the remaining ones survive and continue to grow to a critical size and float to the surface of the melt. Hence, the hydrogen dissolved in the melt is released into the environment. The threshold vibration amplitude of ultrasonic cavitation in the aluminum melt was experimentally measured to be 10–11 µm via direct chill casting [28]. With the presence of nanoparticles, the cavitation threshold should be further smaller. The applied

ultrasonic vibration amplitude in this UA-WAAM process is around 14.6um, which exceeds the threshold value. Additionally, ultrasonic intensity can be calculated through the following equation [29]:

$$I = \frac{1}{2} \rho c (2\pi f A)^2$$

where  $\rho$  is the density of aluminum melt which is about 2375 kg.m $^{-3}$  at 660 °C, c is the sound traveling speed in the aluminum melt which is about 1300 m.s $^{-1}$ , f is the ultrasonic frequency, and A is the ultrasonic vibration amplitude. The estimated ultrasonic intensity of the current UA-WAAM setup is 495 W.cm $^{-2}$ , which greatly exceeds the reported threshold intensity of around 80 W/cm $^2$  [30] in molten aluminum, hence that of the molten aluminum contains nanoparticles.

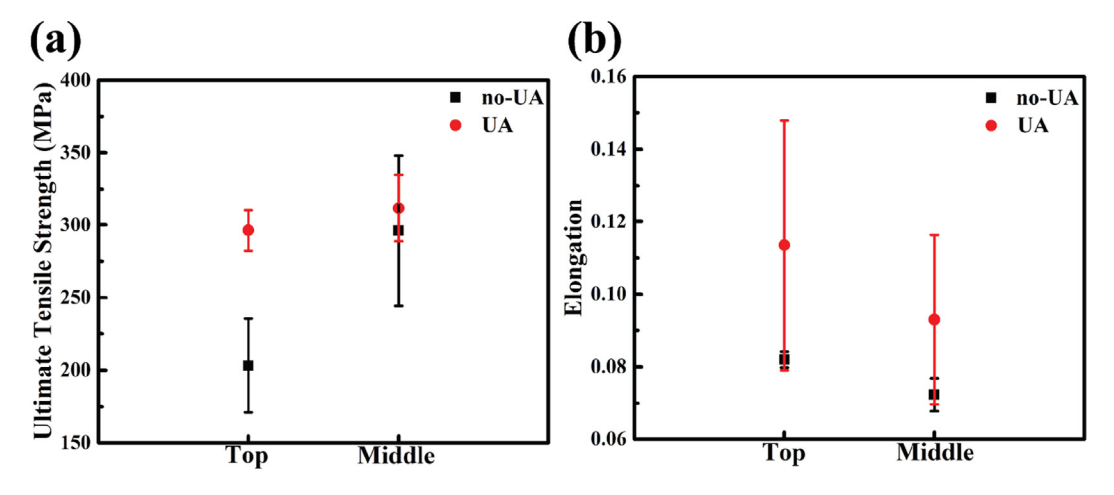


Fig. 9. Tensile test results in top and middle region of the UA and no-UA samples: (a) Tensile strength and (b) Elongation.

#### 4.2. Ultrasonic-assisted dispersion of nanoparticles

Ultrasonic vibration has been one of the popular approaches in ex situ MMNCs fabrications as it can effectively enhance the dispersion of nanoparticles and their wettability with the metal matrix. During the collapse phase of cavitation bubbles, spots with transient high temperature and pressure are produced. These implosive impacts break up the agglomerated nanoparticles. Besides, cavitation can desorb the gaseous phases on the particle surface, thus further improving the wettability characteristics. This promotes effective bonding between TiB2 nanoparticles and the matrix during solidification. Another phenomenon that can possibly contribute to nanoparticles distribution is the ultrasonic capillary effect, which describes the greatly increased penetration of liquid into a capillary or a gap under the applied acoustic field [31]. During the solidification, two adjacent dendrites undergo competing growth and form a capillary in between. Nanoparticles on the solidification front tend to be ejected into this capillary and form clusters. Ultrasonic capillary effect enhances the penetrating motion of the molten metal into the capillary, which together with the hydrodynamic flows caused by acoustic streaming transports the nanoparticles into the bulk liquid melt and improves the dispersions.

In the UA-WAAM setup in this study, the configuration of the ultrasonic probe in the local deposition pool resembles that of the ultrasonically assisted MMNC fabrication system [4]. Accordingly, nanoparticles can be better dispersed with improved wettability based on similar mechanisms. As shown in Figs. 6 and 7, the aggregated TiB<sub>2</sub> clusters at the grain boundaries in no-UA samples were eliminated with UA.

#### 4.3. Effect of UA and nanoparticles on microstructure

Ultrasonic vibration, nanoparticles, and their interactions contributed to the microstructure refinement in this UA-WAAM process. The mechanism of ultrasonic grain refinement is mainly related to the acoustic cavitation and acoustic streaming phenomena, which facilitate dendrite fragmentation and provide additional heterogeneous nucleation sites. Acoustic cavitation bubbles experience a series of stages of initiation, growth, pulsating, and collapse [32]. The intense pressure after bubble collapse induces strong convective flow near the solidification front and the melt flows from liquid zone to mushy zone, which remelts the dendrite roots. According to the high-speed imaging of deep-etched crystals under ultrasonic processing in distilled water [33], acoustic cavitation can fragment dendrites through three main mechanisms: fati-

gue failure from the cyclic pressure of the pulsating bubbles, fast fracture as well as normal bending fracture under the pressure arising from the collapse of the bubbles. Wang et al. [34] performed in situ synchrotron X-radiography to directly observe fragmentation of primary intermetallic during ultrasonic melt processing of Al-35 %Cu alloys in real-time. It was observed that the acoustic streaming also contributed to the dendrite fragmentation by mechanically swaying dendrites as well as transporting hot liquid to remelt dendrite roots. The detached fragmented dendrites also act as effective heterogeneous nuclei for subsequent growth of equiaxed dendrites. The effect of ultrasonic vibration on the grain refinement of an Mg alloy was studied and a proposed mechanism emphasized that acoustic streaming improved the extraction of latent heat and lowered the temperature gradient around the Solid/Liquid (S/L) surface [35]. Therefore, the degree of supercooling was increased and led to the development of refined equiaxed grains.

Effects of nanoparticles in refining solidification structure were discussed [15,36]: the nanoparticles weakened the diffusion of solutes and hence enhanced the constitutional supercooling around the region in front of the solid-liquid interface. As a result, the epitaxial growth of columnar dendrites is decelerated. Besides, nanoparticles can serve as heterogeneous nuclei as TiC nanoparticles were found in the center of grains [37]. Thus, instead of large columnar grains, the growth of equiaxed grains predominate. Furthermore, improved wetting of nanoparticles in the melt activates them to be more effective sites for heterogeneous nucleation [29]. In the UA-WAAM process in this study, since a better dispersion and enhanced wettability of nanoparticles was achieved, contributions of nanoparticles in grain refinement were more significant in the UA sample. Furthermore, as nanoparticles also act as heterogeneous nuclei for secondary precipitates, a more uniform distribution of nanoparticles can accordingly lead to refined secondary phases.

During additive manufacturing, the as-deposited layers will experience remelting and reheating thermal cycles, which leads to a procedure of re-solidification, recovery, grain growth, and artificial aging. UA enhances the more homogeneous dispersion of nanoparticles in the grain interior rather than agglomerating along the grain boundaries. These well-dispersed nanoparticles serve as effective obstacles to dislocation and grain boundary movement [38], which reduces the recovery and grain growth kinetics during the following thermal cycles and result in consistent higher KAM values in the grain structure as shown in Fig. 4 (d). While more aggregated nanoparticles at grain boundaries in no-UA sample provide limited enhancing effect and allow grain growth during the

thermal history, as shown in Fig. 4 (a). Moreover, the introduced UA probe in the molten pool acts as a heat dissipation sink and reduces penetration as shown in Fig. 3, which also mitigates the reheating effects.

# 4.4. Mechanical properties and strengthening mechanisms

The UA sample extracted from both top and middle regions showed enhanced mechanical properties than the no-UA one, which can be attributed to the multiple microstructural features improved with ultrasonic assistance. The main strengthening mechanisms of MMNCs include grain refinement, increased dislocation density, the load-bearing effect, and Orowan strengthening [3]. Both TiB<sub>2</sub> nanoparticles and UA contribute to the grain refinement during the solidification in this UA-WAAM process. Strength contribution from refined grains is based on the Hall-Petch relationship. The difference in the thermal expansion coefficient and elastic modulus between matrix and nanoparticles can induce a high amount of GNDs during the thermal cycles of WAAM deposition process. Thus, the higher KAM level as observed in the EBSD results in Fig. 4 contributes to strengthening in the UA sample [39]. The load-bearing effect focuses on the transfer of tensile stress from the metal matrix to the nanoparticle reinforcements which closely depends on their interfacial bonding condition affected by the dispersion, average size, and wettability of TiB<sub>2</sub> nanoparticles. Microstructure characterization of the UA-WAAM sample shows that UA promotes better dispersion of nanoparticles, which contrasts with the aggregated nanoparticles at grain boundaries in the no-UA samples that intensify the stress concentration and deteriorate mechanical properties. Besides, implosive impacts from the collapse of acoustic cavitation bubbles and flow induced by acoustic streaming can improve the wettability of nanoparticles in the aluminum matrix. The UA enhanced cohesion between matrix and nanoparticles effectively improves the load-bearing reinforcement. Orowan strengthening describes the interactions of particles with dislocations, where the fine particles act as pinning spots for dislocations, which increases the yield strength. On the other hand, when the particle size is larger than 5 um. Orowan strengthening plays a limited secondary role [40], which can be the situation for this UA-WAAM built since the nanoparticles are generally in the micro-meter scale and interparticle spacing is large. In sum, synergistic effects of UA, TiB<sub>2</sub> nanoparticles, and their interactions contribute to the better mechanical properties of the UA-

During the building process, layers at different heights are subject to different thermal histories. Layers deposited at the lower height experienced a longer reheating time (middle region in this case). Based on the hardness distribution, the layers possibly went through a grain growth-aging-over aging procedure, which led to a hardness drop in lower layers in the no-UA sample, as shown in Fig. 8 (c). This type of hardness distribution was not observed in the UA sample, which was possibly related to the heat dissipation from the immersed UA probe that reduces reheating effect and retarded grain growth by better dispersion of nanoparticles. Since the top region is subject to the least amount of reheating, which can be treated as an 'as-weld' microstructure without aging, the hardness of the top region is smaller than the middle region. This hypothesis corresponds to the aging response of 7075 alloy [41]. The UA enhancement of the tensile strength and hardness is more significant in the top layers than in the lower layers. This can be considered from two perspectives. First, in the top region, welldispersed nanoparticles can promote the formation of secondary precipitates in the AA7075 matrix and accelerate the aging kinetics based on the dislocation structures surrounding the nanoparticles, which is similar to the mechanisms of the aging effect of carbon nanotubes (CNT)s on AA7075 [42]. Second, in the middle layers,

a larger area fraction of porosity can be the limiting factor in determining the tensile strength, which can impair the multiple enhancements provided by ultrasonic treatment.

#### 5. Conclusion

Ultrasonic benefits on wire arc additive manufacturing of metal matrix nanocomposite were experimentally studied based on a novel UA-WAAM system, where the ultrasonic probe was directly dipped into the molten pool and traveled behind the arc. This study focused on the AA7075 metal matrix with TiB<sub>2</sub> nanoparticles. The main conclusions are the following:

- The feasibility and effectiveness of the UA-WAAM system were demonstrated, which increased the ultrasonic energy efficiency in improving WAAM processes and allowed the building of complex geometries on a large scale without the output power limitations of ultrasonic transducers.
- In situ ultrasonic vibration during WAAM was proved to be capable of reducing the porosity, refining solidification structure, and therefore led to a more uniform dispersion of TiB<sub>2</sub> nanoparticles. These improved microstructure features can be attributed to the acoustic cavitation and streaming flow induced by power ultrasound.
- UA-WAAM samples showed improved mechanical properties in both tensile tests and micro-hardness tests compared with regular WAAM samples. Strength contributions of TiB<sub>2</sub> nanoparticles to the metal matrix were leveraged by UA, as it played a key role in breaking the particle agglomerate and improving the particle wettability.

# **Declaration of Competing Interest**

The authors declare that they have no known competing financial interests or personal relationships that could have appeared to influence the work reported in this paper.

# Acknowledgement

This work was supported by National Science Foundation, United States, CMMI AM Award # 2044526: CAREER: Ultrasonically Assisted Wire Arc Additive Manufacturing of Metal Matrix Nanocomposites for High-strength, Lightweight Structures. The authors would like to acknowledge the technical support provided by Ed Pfeifer. Electron microscopy was performed at the Center for Electron Microscopy and Analysis (CEMAS) at The Ohio State University.

#### References

- [1] L. Ceschini, A. Dahle, M. Gupta, A.E.W. Jarfors, S. Jayalakshmi, A. Morri, F. Rotundo, S. Toschi, R.A. Singh, Aluminum and Magnesium Metal Matrix Nanocomposites, Springer Singapore, Singapore, 2017. https://doi.org/10.1007/978-981-10-2681-2.
- [2] B.S.S. Daniel, V.S.R. Murthy, G.S. Murty, Metal-ceramic composites via in-situ methods, J. Mater. Process. Technol. 68 (2) (1997) 132–155.
- [3] R. Casati, M. Vedani, Metal Matrix Composites Reinforced by Nano-Particles—A Review, Metals. 4 (2014) 65–83, https://doi.org/10.3390/met4010065.
- [4] X. Li, Y. Yang, X. Cheng, Ultrasonic-assisted fabrication of metal matrix nanocomposites, J. Mater. Sci. 39 (9) (2004) 3211–3212, https://doi.org/ 10.1023/B:JMSC.0000025862.23609.6f.
- [5] J. Liu, J. Li, C. Xu, Interaction of the cutting tools and the ceramic-reinforced metal matrix composites during micro-machining: A review, CIRP J. Manuf. Sci. Technol. 7 (2) (2014) 55–70, https://doi.org/10.1016/j.cirpj.2014.01.003.
- [6] C. Yan, L. Hao, A. Hussein, D. Raymont, Evaluations of cellular lattice structures manufactured using selective laser melting, Int. J. Mach. Tools Manuf 62 (2012) 32–38, https://doi.org/10.1016/j.ijmachtools.2012.06.002.

- [7] S.W. Williams, F. Martina, A.C. Addison, J. Ding, G. Pardal, P. Colegrove, Wire + Arc Additive Manufacturing, Mater. Sci. Technol. 32 (7) (2016) 641–647, https://doi.org/10.1179/1743284715Y.0000000073.
- [8] A. Horgar, H. Fostervoll, B. Nyhus, X. Ren, M. Eriksson, O.M. Akselsen, Additive manufacturing using WAAM with AA5183 wire, J. Mater. Process. Technol. 259 (2018) 68–74, https://doi.org/10.1016/j.jmatprotec.2018.04.014.
- [9] M.J. Bermingham, D.H. StJohn, J. Krynen, S. Tedman-Jones, M.S. Dargusch, Promoting the columnar to equiaxed transition and grain refinement of titanium alloys during additive manufacturing, Acta Mater. 168 (2019) 261– 274, https://doi.org/10.1016/j.actamat.2019.02.020.
- [10] B. Wu, Z. Pan, D. Ding, D. Cuiuri, H. Li, J. Xu, J. Norrish, A review of the wire arc additive manufacturing of metals: properties, defects and quality improvement, J. Manuf. Processes 35 (2018) 127–139, https://doi.org/ 10.1016/j.jmapro.2018.08.001.
- [11] J. Gu, J. Ding, S.W. Williams, H. Gu, P. Ma, Y. Zhai, The effect of inter-layer cold working and post-deposition heat treatment on porosity in additively manufactured aluminum alloys, J. Mater. Process. Technol. 230 (2016) 26– 34, https://doi.org/10.1016/j.jmatprotec.2015.11.006.
- [12] P.A. Colegrove, J. Donoghue, F. Martina, J. Gu, P. Prangnell, J. Hönnige, Application of bulk deformation methods for microstructural and material property improvement and residual stress and distortion control in additively manufactured components, Scr. Mater. 135 (2017) 111–118, https://doi.org/ 10.1016/i.scriptamat.2016.10.031.
- [13] W. Stopyra, K. Gruber, I. Smolina, T. Kurzynowski, B. Kuznicka, Laser powder bed fusion of AA7075 alloy\_ Influence of process parameters on porosity and hot cracking, Addit. Manuf. (2020) 15.
- [14] H. Choi, W.-H. Cho, H. Konishi, S. Kou, X. Li, Nanoparticle-Induced Superior Hot Tearing Resistance of A206 Alloy, Metall and Mat Trans A. 44 (4) (2013) 1897– 1907, https://doi.org/10.1007/s11661-012-1531-8.
- [15] M. Sokoluk, C. Cao, S. Pan, X. Li, Nanoparticle-enabled phase control for arc welding of unweldable aluminum alloy 7075, Nat Commun. 10 (2019) 98, https://doi.org/10.1038/s41467-018-07989-y.
- [16] T.-C. Lin, C. Cao, M. Sokoluk, L. Jiang, X. Wang, J.M. Schoenung, E.J. Lavernia, X. Li, Aluminum with dispersed nanoparticles by laser additive manufacturing, Nat Commun. 10 (2019) 4124, https://doi.org/10.1038/s41467-019-12047-2.
- [17] G.I. Eskin, Broad prospects for commercial application of the ultrasonic (cavitation) melt treatment of light alloys, Ultrason. Sonochem. 8 (3) (2001) 319–325, https://doi.org/10.1016/S1350-4177(00)00074-2.
- [18] W. Chen, Y. Chen, T. Zhang, T. Wen, Z. Yin, X. Feng, Effect of Ultrasonic Vibration and Interpass Temperature on Microstructure and Mechanical Properties of Cu-8Al-2Ni-2Fe-2Mn Alloy Fabricated by Wire Arc Additive Manufacturing, Metals. 10 (2020) 215, https://doi.org/10.3390/met10020215.
- [19] C.J. Todaro, M.A. Easton, D. Qiu, D. Zhang, M.J. Bermingham, E.W. Lui, M. Brandt, D.H. StJohn, M. Qian, Grain structure control during metal 3D printing by high-intensity ultrasound, Nat Commun. 11 (2020) 142, https://doi.org/10.1038/s41467-019-13874-z.
- [20] D. Yuan, S. Shao, C. Guo, F. Jiang, J. Wang, Grain refining of Ti-6Al-4V alloy fabricated by laser and wire additive manufacturing assisted with ultrasonic vibration, Ultrason. Sonochem. 73 (2021) 105472, https://doi.org/10.1016/j. ultsonch.2021.105472.
- [21] H. Ye, K. Ye, B.-G. Guo, F.-B. Le, C. Wei, X.u. Sun, G.-Y. Wang, Y. Liu, Effects of combining ultrasonic micro-forging treatment with laser metal wire deposition on microstructural and mechanical properties in Ti-6Al-4V alloy, Mater. Charact. 162 (2020) 110187, https://doi.org/10.1016/ i.matchar.2020.110187.
- [22] T. Yuan, S. Kou, Z. Luo, Grain refining by ultrasonic stirring of the weld pool, Acta Mater. 106 (2016) 144–154, https://doi.org/10.1016/j. actamat.2016.01.016.
- [23] K.F. Ayarkwa, S.W. Williams, J. Ding, Assessing the effect of TIG alternating current time cycle on aluminium wire + arc additive manufacture, Addit. Manuf. 18 (2017) 186–193, https://doi.org/10.1016/j.addma.2017.10.005.
- [24] J. Kang, X. Liu, M. Xu, Plastic deformation of pure copper in ultrasonic assisted micro-tensile test, Mater. Sci. Eng., A 785 (2020) 139364, https://doi.org/ 10.1016/j.msea.2020.139364.

- [25] Z. Zribi, H.H. Ktari, F. Herbst, V. Optasanu, N. Njah, EBSD, XRD and SRS characterization of a casting Al-7wt%Si alloy processed by equal channel angular extrusion: Dislocation density evaluation, Mater. Charact. 153 (2019) 190–198, https://doi.org/10.1016/j.matchar.2019.04.044.
- [26] R. Petrov, L. Kestens, A. Wasilkowska, Y. Houbaert, Microstructure and texture of a lightly deformed TRIP-assisted steel characterized by means of the EBSD technique, Mater. Sci. Eng., A 447 (1-2) (2007) 285–297, https://doi.org/ 10.1016/j.msea.2006.10.023.
- [27] G.I. Eskin, Cavitation mechanism of ultrasonic melt degassing, Ultrason. Sonochem. 2 (2) (1995) S137–S141, https://doi.org/10.1016/1350-4177(95) 00020-7
- [28] S. Komarov, K. Oda, Y. Ishiwata, N. Dezhkunov, Characterization of acoustic cavitation in water and molten aluminum alloy, Ultrason. Sonochem. 20 (2) (2013) 754–761, https://doi.org/10.1016/j.ultsonch.2012.10.006.
- [29] G.I. Eskin, D.G. Eskin, Ultrasonic Treatment of Light Alloy Melts, CRC Press,
- [30] G. Wang, Q. Wang, M.A. Easton, M.S. Dargusch, M. Qian, D.G. Eskin, D.H. StJohn, Role of ultrasonic treatment, inoculation and solute in the grain refinement of commercial purity aluminium, Sci Rep. 7 (2017) 9729, https://doi.org/10.1038/ s41598-017-10354-6.
- [31] A.K. Gilmutdinov, A.I. Gorunov, O.A. Nyukhlaev, M. Schmidt, Investigations of the sound frequency effect on laser acoustic welding of stainless steel, Int J Adv Manuf Technol. 106 (7-8) (2020) 3033–3043, https://doi.org/10.1007/s00170-019-04825-5
- [32] D.G. Shchukin, E. Skorb, V. Belova, H. Möhwald, Ultrasonic Cavitation at Solid Surfaces, Adv. Mater. 23 (17) (2011) 1922–1934, https://doi.org/10.1002/ adma.201004494.
- [33] F. Wang, I. Tzanakis, D. Eskin, J. Mi, T. Connolley, In situ observation of ultrasonic cavitation-induced fragmentation of the primary crystals formed in Al alloys, Ultrason. Sonochem. 39 (2017) 66–76, https://doi.org/10.1016/j. ultsonch.2017.03.057.
- [34] F. Wang, D. Eskin, J. Mi, C. Wang, B. Koe, A. King, C. Reinhard, T. Connolley, A synchrotron X-radiography study of the fragmentation and refinement of primary intermetallic particles in an Al-35 Cu alloy induced by ultrasonic melt processing, Acta Mater. 141 (2017) 142–153, https://doi.org/10.1016/j.actamat.2017.09.010.
- [35] X. Liu, Y. Osawa, S. Takamori, T. Mukai, Grain refinement of AZ91 alloy by introducing ultrasonic vibration during solidification, Mater. Lett. 62 (17-18) (2008) 2872–2875, https://doi.org/10.1016/j.matlet.2008.01.063.
- [36] M. Sokoluk, J. Yuan, S. Pan, X. Li, Nanoparticles Enabled Mechanism for Hot Cracking Elimination in Aluminum Alloys, Metall Mater Trans A. 52 (7) (2021) 3083–3096, https://doi.org/10.1007/s11661-021-06302-9.
- [37] E. Guo, S. Shuai, D. Kazantsev, S. Karagadde, A.B. Phillion, T. Jing, W. Li, P.D. Lee, The influence of nanoparticles on dendritic grain growth in Mg alloys, Acta Mater. 152 (2018) 127–137, https://doi.org/10.1016/j.actamat.2018.04.023.
- [38] Z. Zhang, D.L. Chen, Contribution of Orowan strengthening effect in particulate-reinforced metal matrix nanocomposites, Mater. Sci. Eng., A 483–484 (2008) 148–152, https://doi.org/10.1016/j.msea.2006.10.184.
  [39] J. Gu, X. Wang, J. Bai, J. Ding, S. Williams, Y. Zhai, K. Liu, Deformation
- [39] J. Gu, X. Wang, J. Bai, J. Ding, S. Williams, Y. Zhai, K. Liu, Deformation microstructures and strengthening mechanisms for the wire+arc additively manufactured Al-Mg4.5Mn alloy with inter-layer rolling, Mater. Sci. Eng., A 712 (2018) 292–301, https://doi.org/10.1016/j.msea.2017.11.113.
- [40] D.J. Lloyd, Particle reinforced aluminium and magnesium matrix composites, Int. Mater. Rev. 39 (1) (1994) 1–23, https://doi.org/10.1179/imr.1994.39.1.1.
- [41] T. Aoba, M. Kobayashi, H. Miura, Effects of aging on mechanical properties and microstructure of multi-directionally forged 7075 aluminum alloy, Mater. Sci. Eng., A 700 (2017) 220–225, https://doi.org/10.1016/j.msea.2017.06.017.
- [42] H.B. Zhang, B. Wang, Y.T. Zhang, Y. Li, J.L. He, Y.F. Zhang, Influence of aging treatment on the microstructure and mechanical properties of CNTs/7075 Al composites, J. Alloy. Compd. 814 (2020) 152357, https://doi.org/10.1016/ i.iallcom.2019.152357.